Pb^{2+}, Cd^{2+} and Hg^{2+} removal by designed functionalized swelling high-charged micas.

F.J. Osuna[a], E. Pavón[a,b] and M.D. Alba[a,1]

[a]*Instituto Ciencia de los Materiales de Sevilla (CSIC-US). Avda. Americo Vespucio, 49. 41092 Sevilla (Spain).*

[b]*Departamento de Física de la Materia Condensada. Universidad de Sevilla. Avda. Reina Mercedes s/n. 41012 Sevilla (Spain).*

Abstract

The increasing accumulation of toxic heavy metals in the environment has generated the need of efficient removal systems, being the adsorption method the most popular one applied in aqueous solutions. Of particular concern is the case of Pb^{2+}, Cd^{2+} and Hg^{2+} due to their high potential hazard. In this paper, we describe the feasibility of a new family of nanomaterials, swelling high charge micas, in the removal of these cations from aqueous solutions. Batch adsorption experiments were carried out in the as-made micas, Na-M*n*, and after functionalization with ethylammonium, EA-M*n*, and mercaptoethylammonium, MEA-M*n*. The results have demonstrated that all of them are efficient heavy metal adsorbents, being Na-M2 the best adsorbent for Pb^{2+} and Cd^{2+}, and, MEA-M2 for Hg^{2+}.

Keywords. swelling mica, heavy metals, pollutant, adsorption, functionalized adsorbents, thiol

[1] Corresponding author.
E-mail address: alba@icmse.csic.es

1. Introduction

Industrialization has led to the accumulation in the environment of toxic heavy metals, such as Cr^{6+}, Ni^{2+}, Pb^{2+}, Hg^{2+} and Cd^{2+}, causing severe environmental problems and damaging human health (Volesky, 1990; Yuan et al., 2020; Zhang et al., 2020). Among them, Pb^{2+}, Cd^{2+} and Hg^{2+} stand out due to their high potential hazard and their presence in soils and close to aqueous effluents (Sun et al., 2020; Volesky, 1990). Conventional methods such as soil washing (Sierra et al., 2010), cement-based solidification/stabilization (Shen et al., 2019), containment (NJDEP, 2014) and electrokinetic removal (Figueroa et al., 2016) have been used for the remediation of soils with heavy metals contamination. However, great efforts are still demanding to remove them from contaminated water and wastewater (Bailey et al., 1999; Farid et al., 2020; Inglezakis et al., 2007; Shaikhiev et al., 2020).

Adsorption is highlighted as one of the preferred methods for the elimination of toxic contaminants (heavy metals, among others) from aqueous systems, being an effective and economic technique for their removal, recovery and recycling. Several materials have been tested to maximise the adsorption capacity of heavy metal cations (Tran et al., 1999). Conventional adsorbents such as granular or powdered activated carbon are technically inefficient and economically unviable. Consequently, non-conventional materials (Ezzat et al., 2020; Shaikh, 2020; Shaikhiev et al., 2020), such as synthetic and natural fly ash (Mathur and Rupainwar, 1988; Yang et al., 2020), lignite (Balasubramanian and Ahamed, 2000), tree fern (Ho, 2003), peanut shell (Periasamy, K, Namasivayam, 1994) or peat (Ho, Y S, Ng, J C Y, McKay, 2001) have been used for this purpose.

Clay minerals are widely used as adsorbents as they are the major soil constituents and act as natural scavengers for pollutants in water through both ion exchange and

adsorption mechanisms. Moreover, their compositional and structural characteristics are crucial for their adsorption capacities. First, cation exchange capacity (CEC) is different for each clay minerals and determines their adsorption capacity through this mechanism (Grim, 1968). Second, the location of isomorphous substitution in the clay layer is an important factor affecting both hydration and cation speciation in the interlayer space, determining the strength of the Lewis base (Malferrari et al., 2007).

Alba et al. (Alba et al., 2006) have synthetized a new family of clay minerals that has been demonstrated to be attractive adsorbents. These synthetic fluorophlogopites have layer charge in the range of the brittle micas but unlike the natural ones, they exhibit swelling properties and cation exchange capacity (Naranjo et al., 2014). Those as-made micas, Na-M*n* (*n* is the layer charge which derives from the tetrahedral Si^{+4}/Al^{+3} substitutions and can be found between 2 and 4), have exhibited excellent capacity for the removal of radioactive cations and organic pollutants from wastewater (Alba et al., 2006; García-Jiménez et al., 2016; Osuna et al., 2019b, 2018; Pazos et al., 2017) and are promising materials for heavy metal removal, although their efficiency has not been proven yet.

However, raw clay minerals have shown poor stabilization performance, as the immobilized metals can be exchanged and released in the long term (Ugochukwu et al., 2013). Then, in order to improve their adsorption capability, their surfaces have been functionalized by inserting functional groups and organic molecules such as alkylammonium cations (Bhattacharyya and Sen Gupta, 2008; Osuna et al., 2019b; Pazos et al., 2017), L-cystein (Mittal et al., 2016) and humic acid (Wu et al., 2011). In fact, different adsorption sites are observed when the functionalization is produced by grafting organic groups, mainly thiol or amine functional groups (Cruz-Guzman et al., 2006; Lin and Juang, 2002; Malferrari et al., 2007; Mercier, L, Detellier, 1995; Shah et al., 2005).

Therefore, the aim of the present study was, on the one hand, to investigate the feasibility of using a family of design swelling high-charge micas, Na-M*n*, before and after the functionalization with ammonium and thiol groups, for removal of Pb^{2+}, Cd^{2+} and Hg^{2+} from aqueous solution and, on the second hand, to analyse the different removal mechanisms.

2. Materials and methods

2.1. Materials

As-made Na-M*n* (*n* is the layer charge equals to 2 or 4) were synthetized by mixing SiO_2, Al_2O_3, MgF_2, and NaCl in the molar ratio 8-*n*:*n*:6:2*n*. The starting materials were SiO_2 from Sigma (CAS no. 112945-52-5, 99.8% purity), $Al(OH)_3$ from Sigma Aldrich (CAS no. 21645-51-2, 99% purity), MgF_2 from Aldrich (CAS no. 20831-0, 98% purity), and NaCl from Panreac (CAS no. 131659, 99.5% purity). All reagents were mixed and ground in an agate mortar and heated up to 900 °C for 15 h in a Pt crucible. Finally, the solids were washed with deionized water and dried at room temperature (Alba et al., 2006)

The chemical products used for the preparation of the organoclays were obtained from Aldrich Chemical Co. 600 mg of mica was added to ethylammonium (EA: $C_2H_5NH_3^+$) or mercaptoethylammonium (MEA: $SHC_2H_4NH_3^+$) solutions, assuring their concentration, twice mica cation exchange capacity, in order to favour the cation exchange reaction. They were left to react for 3h at 80 ºC. The solids were recovered by centrifugation, washed with deionized water and ethanol and dried at room temperature. The functionalized micas were named as EA-M*n* or MEA-M*n* (Osuna et al., 2019a).

2.2. Batch adsorption

Adsorption experiments were carried out at RT and prepared in a 50 ml centrifuge tube, where 0.5 g of Y-M*n* (Y= Na, EA or MEA and *n*=2 or 4) were dispersed with 50 ml of a 25 mM $X(NO_3)_2$ ($X=Pb^{2+}$, Cd^{2+} or Hg^{2+}) solution. Adsorption of Pb^{2+} and Cd^{2+} was performed at their natural pH as showed in Fig. S1 (open stars). The pH of the initial $Hg(NO_3)_2$ solution was adjusted to 1.5 to avoid the salt precipitation. The samples were equilibrated for 4 weeks in an end-over-end shaker at 50 rpm. Afterwards, the phases were separated by centrifugation at 10,000 rpm at 8 ºC for 25 min. The samples were named as X-Y-M*n*.

The supernatants were filtered by a 0.2 μm syringe filter. After measuring the pH and E_h values, the solutions were preserved by adding HNO_3 and cool stored for subsequent a Na^+ and heavy metal analysis of three aliquots by inductively coupled plasma-mass spectrometry (ICP-MS); the difference for metals before and after the adsorption reveals the amount of adsorbed metals (C_s, meq/kg):

$$C_s = \frac{C_i \cdot V_i - C_{eq} \cdot V_{eq}}{m}$$

and the desorbed Na^+ (C_{des}, meq/kg) is calculated as following:

$$C_{des} = \frac{C_{i(Na^+)} \cdot V_i - C_{eq(Na^+)} \cdot V_{eq}}{m}$$

V_i (L) is the volume of the initial solution, V_{eq} (L) is the volume of the supernatant, m is mica weight (kg), C_i (meq/L) and C_{eq} (meq/L) are the concentration of the metals in the initial and final solutions (Table S1), respectively. The errors on the concentration have been calculated from the triplicate ICP-MS analysis.

Solids were dried at room temperature and characterized by X-ray diffraction (XRD), ATD/TG and MAS-NMR spectroscopy.

2.3. Characterization

The electromotive force (E_h) and the pH values of the initial solutions and supernatants were measured at room temperature using a Eutech Instruments PC 700 pH-meter.

ICP-MS (Inductively Coupled Plasma-Mass Spectrometry) was used to analyse, on the one hand, the sulphur content on the X-MEA-M*n* solid samples, and, on the other hand, the metal content on the initial solutions and the supernatants obtained after the equilibrium reaction. Measurements were carried out at the Microanalysis Laboratory (CITIUS, University of Seville, Spain) using a HORIBA JOBIN YVON-ULTIMA 2 equipment.

Thermogravimetrial (TG/DTA) experiments were carried out using a TA (model STD-Q600) instrument, in Characterization Service (CITIUS, University of Seville, Spain), with alumina as reference. The samples were placed into a Pt crucible and maintained at air throughout the heating period. The temperature was increased at a constant rate of 10° C/min up to 1000 ºC.

Powder X-ray diffraction (XRD) was carried out to check the phase purity, to monitor crystallinity and to determine the basal spacing of the micas. XRD patterns were obtained at the X-ray laboratory (CITIUS, University of Seville, Spain) on a Bruker D8 Advance instrument equipped with a Cu K_α radiation source operating at 40 kV and 40 mA. Diffractograms were obtained in the 2θ range of 3–70° with a step size of 0.015° and a step time of 0.1 s.

Solid state nuclear magnetic resonance (MAS-NMR) was used to analyse the short order range in the solid interlayer space. Single-pulse (SP) MAS-NMR experiments were recorded on a Bruker AVANCE WB400 spectrometer equipped with a multinuclear probe, at the Nuclear Magnetic Resonance Service of University of Córdoba (Córdoba, Spain). Powdered samples were packed in 3.2 mm zirconia rotors and spun at 10 kHz.

149 ^{23}Na MAS NMR spectra were recorded at 105.84 MHz with a pulse width of 0.75 μs (π/2
150 pulse length = 4.5 μs) and a delay time of 0.1 s. ^{13}C MAS NMR spectra with proton
151 decoupling were recorded at 104.26 MHz with a pulse width of 2.5 μs (π/2 pulse length
152 = 7.5 μs) and a delay time of 2 s. The chemical shift values were reported in ppm from
153 tetramethylsilane for ^{13}C and from a 0.1 M NaCl solution for ^{23}Na.
154
155 **3. Results**
156 The pH and E_h values for the initial and supernatant solutions were represented in
157 the Pourbaix diagrams (Fig. S1), showing the most stable species in the solutions.
158 In all the initial solutions, the divalent heavy metal cation (X^{2+}) was the most
159 stable species, although in mercury solutions the pH and E_h values were close to the Hg_2^{2+}
160 stability region.
161 In general, supernatants had a less acidic pH and a lower E_h than the starting
162 solutions. Despite these changes, the most stable species in lead and cadmium
163 supernatants was still the X^{2+} cation. However, HgO was the most stable species in Hg-
164 Na-M*n* and Hg-EA-M*n* supernatants. The decrease in E_h in Hg-MEA-M*n* supernatants
165 was more evident than in Hg-Na-M*n* supernatants, causing pH and E_h values to be close
166 to the HgO/ Hg_2^{2+} stability limit for Hg-MEA-M4 and between HgO and metallic Hg for
167 Hg-MEA-M2 (Fig. S1).
168 The concentration of sodium and heavy metal cations in the initial solutions and
169 supernatants was measured by ICP-MS (Table S1). The desorbed interlayer sodium (C_{des}
170 (Na^+)) and adsorbed heavy metal cations (C_s (X^{2+})) in each system were calculated from
171 these values (Fig. 1). Interlayer sodium was not completely desorbed in Na-M*n* (Fig. 1,
172 upper). As an exception, Hg-Na-M2 desorbed a quantity of sodium cations greater than
173 its cation exchange capacity (CEC), probably due to the low pH value of the starting Hg^{2+}

174 solution that provoked the desorption of the non-exchanged sodium (Osuna et al., 2019b).
175 In both sodium micas, the values of adsorbed heavy metal cations were higher than
176 desorbed sodium. Thus, other adsorption mechanisms further than cation exchange may
177 be happening, such as the formation of precipitates and/or adsorption at specific sites.

178 Fig. 1, bottom, compares the adsorption data for each heavy metal cation on the
179 different adsorbents. EA-M*n* adsorbed less Pb^{2+} and Hg^{2+} than Na-M*n*. The adsorbed Cd^{2+}
180 was higher in EA-M4 and similar in EA-M2 in comparison with Na-M*n*. The system that
181 adsorbs the least amount of Pb^{2+} and Cd^{2+} was MEA-M*n*. In contrast, the amount of
182 adsorbed Hg^{2+} in MEA-M*n* was higher than in the other two systems.
183 It should be noted that the Y-M2 systems (Y = Na, EA and MEA) adsorbed an amount of
184 Hg^{2+} higher than the CEC of Na-M2.

185 In order to analyze possible changes in the structure of the adsorbents and identify
186 new crystalline phases, solid samples were analyzed by XRD.
187 Fig. 2 compares the XRD diagrams in the 2θ range 4-10º of Na-M*n* before and after each
188 adsorption. The adsorption of Pb^{2+}, Cd^{2+} and Hg^{2+} in Na-M4 did not produce changes in
189 the hydration state of the sheets. The XRD diagram of sample Pb-Na-M2 showed a unique
190 *001* reflection to ca. 1.21 nm, same basal spacing than sodium mica whereas Cd-Na-M2
191 and Hg-Na-M2 XRD patterns showed a second reflection corresponding to a greater basal
192 spacing (1.45 nm) than Na-M2 (1.21 nm). This peak was compatible with the presence of
193 heavy metal cations or leached framework cations surrounded by a bilayer of water in the
194 interlayer space(Kodama and Komarneni, 1999). This layer swelling after the adsorption
195 of Cd^{2+} and Hg^{2+} did not occur in Na-M4. Na-M4 had a greater layer charge than Na-M2
196 and, therefore, a higher interaction between the interlayer cations and the surface of the
197 mica occurred, hindering the swelling capacity.

198 The XRD patterns of the EA-M*n* before and after each adsorption were shown in
199 Fig. 3. EA-M4 XRD pattern (Fig. 3a, left) showed a single reflection due to the parallel
200 bilayer arrangement of the organic cation (1.60 nm) (Osuna et al., 2019a). The adsorption
201 of Pb^{2+} did not produce variation in the *001* reflection. In the case of EA-M4 after
202 adsorbing Cd^{2+}, in addition to the reflection at 1.60 nm, a second less intense reflection
203 was observed at 1.22 nm. This basal spacing was compatible with the presence of organic
204 cations in a parallel monolayer or Cd^{2+} arrangement surrounded by a monolayer of water
205 (Osuna et al., 2019a). The Hg-EA-M4 XRD pattern showed a single reflection at a value
206 of 2Θ that corresponds to a basal spacing of 1.36 nm, lower than that of the adsorbent (ca.
207 1.60 nm). This basal distance may be related to the presence of hydrated mercury cations
208 in the interlayer or to organic cations arranged in parallel monolayer (Osuna et al., 2019a).
209 These changes in the hydration states indicated that the adsorption of cadmium and
210 mercury cations occurs by a partial exchange of organic cations. In the case of Pb^{2+}, the
211 XRD patterns could indicate that a large amount of EA was not desorbed.
212 The XRD pattern of EA-M2 (Fig. 3, right) showed two reflections due to different
213 arrangements of the organic cation: in parallel bilayer (ca. 1.60 nm) and parallel
214 monolayer (ca. 1.26 nm) (Osuna et al., 2019a). After the adsorption of Pb^{2+}, there were
215 no changes in the reflections, however, after the adsorption of Cd^{2+}, a decrease in the
216 intensity of the reflection at ca. 1.60 nm was observed and the reflection at ca. 1.26 nm
217 disappeared. A new reflection could also be observed at ca. 1.45 nm that could be
218 attributed to Cd^{2+} surrounded by a bilayer of water (Kodama and Komarneni, 1999). This
219 could indicate that the adsorption of Cd^{2+} was produced by an exchange of the EA
220 molecules by the heavy metal cation. In the case of Hg^{2+}, the XRD pattern showed two
221 reflections, one at ca. 1.21 nm that may correspond to a parallel monolayer arrangement
222 of EA or to Hg^{2+} surrounded by a monolayer of water. The second reflection at 1.36 nm,

223 the same interlayer spacing than Hg-EA-M4, was due to a higher degree of hydration of
224 Hg^{2+} or to organic cations arranged in parallel monolayer (Osuna et al., 2019a).
225 In the case of Y-MEA-M4, the XRD patterns (Fig. 4, left) showed the same *001*
226 reflections than the adsorbent: an intense reflection compatible with the organic cations
227 arranged in parallel bilayer (ca. 1.60 nm) and a second low intensity *001* reflection at ca.
228 1.37 nm due to the organic cations arranged in a parallel monolayer (Osuna et al., 2019a).
229 The XRD pattern of MEA-M2 (Fig. 4a, right) showed three basal spacings due to different
230 configurations of the organic cation: parallel bilayer (ca. 1.63 nm) and non-parallel
231 monolayer (ca 1.57 nm and 1.46 nm) (Osuna et al., 2019a). After each adsorption, the
232 XRD patterns (Fig. 4b-d, right) showed the reflections corresponding to the arrangement
233 in parallel bilayer (ca. 1.60 nm) and non-parallel monolayer (1.57 nm). However, a
234 decrease in the relative intensity of the reflection at ca. 1.60 nm with respect to the
235 adsorbent was observed. This decrease was greater in the adsorption of Hg^{2+} than in that
236 of Cd^{2+}, and greater in this than when adsorbing Pb^{2+}. Furthermore, the reflection at ca.
237 1.47 nm, due to organic cations in a non-parallel monolayer configuration, was not
238 detected. This could indicate that some amount of MEA was desorbed from the solid
239 during the adsorption reaction.
240 The presence of new crystalline phases in the adsorbents after each adsorption was
241 analyzed by XRD in the 10º-70º 2Θ range, Fig. S2-S4. The XRD patterns of the Na-M*n*
242 samples (Fig. S2) showed the presence of PbF_2 in Pb-Na-M*n* and $Hg(NO_3)_2$ in Hg-Na-
243 M*n*. PbO was also observed in Pb-Na-M2. The presence of this species is in accordance
244 with the Pourbaix diagram, which indicated that the most stable species in the Pb-Na-M2
245 supernatants is PbO (Fig. S1). No new crystalline phases were observed in Cd-Na-M*n*.
246 The formation of the crystalline phases that contain lead and mercury explained that the

247 adsorbed amount of these two heavy metals was greater than that of Cd^{2+} in both sodium
248 micas.

249 The XRD patterns of Pb-EA-M*n* (Fig. S3b) and Pb-MEA-M4 (Fig. S4b, upper)
250 indicated the presence of $Pb(NO_3)_2$. No new crystalline phases were observed in Pb-
251 MEA-M2 (Fig. S4b, bottom). No new phases were observed in the functionalized micas
252 after adsorbing Cd^{2+} (Fig. S3c and S4c) or Hg^{2+} (Fig. S3d and S4d).

253 Fig. S5 compared the DTG curves of all samples before and after adsorbing each
254 heavy metal cation. Two zones could be differentiated in these curves:
255 - Zone I (25-150 ° C (Hg^{2+}) / 25-230 ° C (Pb^{2+}/Cd^{2+})): the weight loss was due to the loss
256 of coordination water.
257 - Zone II (150-850 ° C (Hg^{2+}) / 230-850 ° C (Pb^{2+}/Cd^{2+})): the weight loss was due to the
258 decomposition of organic matter and/or volatilization of adsorbed heavy metal cations.

259 In general, the first zone of the DTG curve was characterized by one or two mass
260 losses corresponding to the elimination of water from the different hydration spheres of
261 the interlayer cation. After adsorption, the removal of the coordinating water molecules
262 occurred at higher temperatures than in the adsorbents. The analysis of the loss of mass
263 by thermogravimetry (TG) in this range allowed obtaining the amount of water per kg of
264 sample (Table 1).

265 In the cases of Pb-Na-M*n* and Pb-MEA-M*n*, the amount of coordination water
266 was similar to that calculated for the adsorbent materials. In the case of Pb-EA-M2, the
267 amount of water increased after adsorption, while in the Pb-EA-M4, the amount of
268 adsorbed water was lower than in EA-M4. In general, the samples with cadmium had a
269 greater amount of water than their adsorbents, this increase being more significant in the
270 samples Na-M2 and EA-M2. This greater amount of water agreed with reflections *001* to
271 ca. 1.45 nm observed on the Cd-Na-M2 and Cd-EA-M2 XRD patterns. The mercury

adsorption produced different changes for water amount depending on the adsorbent. Both Hg-Na-M*n* micas had a lower amount of coordination water. However, the Hg-EA-M2 sample had a higher amount of water than the EA-M2, which was consistent with the reflection at 1.45 nm observed in the XRD pattern. In contrast, Hg-MEA-M2 contained slightly less water than the adsorbent. Regarding both Hg-EA-M4 and Hg-MEA-M4, the same amount of coordination water before and after adsorption was observed.

The decomposition of organic cations and/or volatilization of heavy metal cations occurred during the second zone of the DTG curve (Hu, G, Liu, G, Wu, D , Fu, 2018; Malferrari et al., 2006; Praus et al., 2012) and the temperature and processes that occurred in this zone depend on the nature of the heavy metal cation (Fig. S5). In Pb-Na-M*n*, the loss of mass was minimal and similar to that of sodium micas before adsorption.

In the DTG curve of Pb-EA-M4, the removal of the organic cation occurred in three stages between 300 °C and 500 °C. The DTG curve of Pb-EA-M2 showed signals with low intensity in that temperature range, denoting that mica contained a small amount of EA due to the cation exchange adsorption between Pb^{2+} and the organic cation. Unlike the EA functionalized micas, the DTG curves of the Pb-MEA-M*n* presented a profile similar to those of the adsorbents, indicating that the adsorption of Pb^{2+} did not produce changes in thermal stability of the organic cation.

The DTG curves of Cd-Na-M*n* showed a small loss of mass at ca. 350 °C. In the literature, this mass loss was attributed to the removal of coordinating water from CdO (Fahim and Kolta, 1970). This cadmium phase was amorphous since it could not be observed in the corresponding XRD pattern. In the case of Cd-EA-M4, a small loss of mass occurred at 390 °C and corresponded to the removal of the interlayer EA. However, in the DTG curve of Cd-EA-M2, the characteristic EA decomposition signals were not distinguishable, which indicated that mica contained very small amount of organic

297 cations. This fact agreed with the XRD pattern (Fig. 3c, right), which showed a main
298 reflection attributable to the interlayer hydrated Cd^{2+} and the disappearance of the
299 characteristic reflections of the EA in the interlayer. No changes in the DTG curve of
300 MEA functionalized micas (Fig. S5) were observed after adsorbing Cd^{2+}, due to the low
301 amount of adsorbed cation (Fig. 1).

302 In the 150-850 ° C range, the DTG curve of the Hg-Na-M4 showed two mass
303 losses attributed to the elimination of Hg^{2+}. The first loss at 350 °C was due to the removal
304 of mercury cations that form external sphere complexes (exchangeable mercury) (Hu, G,
305 Liu, G, Wu, D , Fu, 2018; Malferrari et al., 2006; Praus et al., 2012). Mercury cations
306 forming internal sphere complexes vaporized at a higher temperature (ca. 550 °C), since
307 the adsorption force was greater as they are coordinated with the basal oxygens (Hu, G,
308 Liu, G, Wu, D , Fu, 2018; Malferrari et al., 2006; Praus et al., 2012). The elimination of
309 exchangeable mercury in Hg-Na-M2 occurred at a lower temperature than in Hg-Na-M4.
310 (ca. 300 °C), as a consequence of the lower layer charge in Na-M2. The loss of mercury
311 adsorbed as internal sphere complexes in Hg-Na-M2 occurred in two stages at ca. 500 °C
312 and 650 °C.

313 The DTG curve of Hg-EA-M*n* (Fig. S5, Table 2) was characterized by a set of
314 three signals: i) elimination of mercury adsorbed on the organic chain, ii) decomposition
315 of organic cation, and, iii) vaporization of exchangeable mercury forming an external
316 sphere complex (Hu, G, Liu, G, Wu, D , Fu, 2018; Malferrari et al., 2006; Praus et al.,
317 2012). The elimination of mercury adsorbed in the organic chain occurred at a higher
318 temperature in the less charged mica (Table 2). As well, the decomposition of EA in Hg-
319 EA-M2 occurred at 430 °C while in Hg-EA-M4 occurred in two phases (290 °C and 445
320 °C), as in EA-M4. The temperature when external sphere complexed mercury evaporates
321 did not depend on the layer charge of the adsorbent. However, Hg^{2+} cations that form

internal sphere complexes were eliminated at a higher temperature in Hg-EA-M4, because its higher layer charge generated more strongly adsorbed cations.

The DTG curves of the Hg-MEA-M*n* (Fig. S5, Table 2) presented the same set of three signals: i) removal of mercury adsorbed on the MEA (ca. 200 °C), ii) decomposition of the organic cation (ca. 270 °C), and, iii) loss of mercury adsorbed at non-specific sites at ca. 340 °C. In addition to these three signals, the Hg-MEA-M2 DTG curve also showed a small signal at 600 °C attributed to the loss of Hg^{2+} cations that form internal sphere complexes.

The analysis of the mass losses obtained by TG would allow calculating the amount of organic cations in the micas (Osuna et al., 2019a). However, in the temperature range in which the organic matter decomposes, other processes such as the vaporization of mercury or the dehydration of CdO also occurred which hindered the calculation. In MEA-M*n*, the amount of sulphur calculated from ICP-MS could help to a correct calculation of the organic matter from TG data. When comparing the data obtained from ICP-MS and TG (Table 3), it was observed that the MEA amount after the adsorption of Pb^{2+} and Cd^{2+} was similar by both techniques, with the values measured by TG being slightly higher. This allowed using the data provided by TG to know, semiquantitatively, the amount of organic cation contained in the X-EA-M*n* samples (X= Pb^{2+} and Cd^{2+}), not so in the case of Hg^{2+}.

As seen in Table 3, all functionalized micas after Pb^{2+} and Cd^{2+} adsorption contained a lower amount of organic cations. This corroborated that the adsorption of heavy metal cations was carried out, at least in part, by cation exchange. The mass loss associated with the decomposition of the organic chain measured by TG in functionalized micas after Hg^{2+} adsorption is much higher than that of adsorbents. This indicated that

346 the organic chain and Hg^{2+} cations loss overlapped and, then, it was impossible to know
347 the amount of EA after Hg^{2+} adsorption.

348 The values of adsorbed heavy metal cations and desorbed interlayer cations in Pb-
349 EA-M2, Cd-EA-M2 and Cd-EA-M4 were similar (Table 4), indicating that adsorption
350 occurred mainly by cation exchange. The adsorbed amount of Pb^{2+} in EA-M4 was higher
351 than that of the desorbed interlayer cations due to the formation of $Pb(NO_3)_2$ precipitates,
352 as observed in the XRD patterns (Fig. 3), and, also to adsorption at specific sites.

353 The amount of Pb^{2+} and Cd^{2+} adsorbed on MEA-M*n* was lower than the amount
354 of the desorbed interlayer cations (C_{des} (EA/MEA + Na^+)) (Table 4), indicating that the
355 cation exchange reaction occurred but part of the layer charge was balanced by hydronium
356 ions or leached framework cations. Regarding the adsorption of Hg^{2+}, the amount of
357 heavy metal adsorbed was much greater than the amount of MEA and Na^+ desorbed in
358 both micas. This could indicate that, in addition to the cation exchange reaction, the
359 adsorption occurred at specific sites (thiol group). This fact agreed with the DTG plots
360 where the signal intensity of Hg^{2+} adsorbed in organic cations in Hg-MEA-M*n* was higher
361 than in Hg-EA-M*n*.

362 The samples were analyzed by ^{23}Na MAS NMR to obtain information about the
363 changes of the interlayer Na^+ after the adsorption processes of heavy metal cations. The
364 ^{23}Na MAS NMR spectra of the samples after the adsorption of each heavy metal (Fig. 5)
365 were generally characterized by three signals: i) a signal between 10 and -30 ppm that
366 corresponded to the hydrated interlayer sodium, ii) a signal to ca. 30 ppm attributed to
367 non-exchangeable sodium, and, iii) a signal at ca. 5 ppm due to sodium in sodalite
368 (Naranjo et al., 2015).

369 The intensity of the hydrated sodium signal decreased in all the samples in
370 accordance with the adsorbed amount of heavy metal cations measured by ICP-MS (Fig.

1). The ^{23}Na MAS NMR spectrum of Y-M2 after each adsorption (Fig. 5) showed a decrease of the non-exchangeable and sodalite signals, according with heavy metal cations adsorbed at specific sites and/or forming precipitates.

The functionalized micas were analyzed by ^{13}C MAS NMR to obtain more information on the changes produced in the organic cations when adsorbing the different heavy metal cations. The ^{13}C MAS NMR spectrum of EA-M4 (Fig. 6a, up left) was characterized by two signals corresponding to the carbons of CH_3 (13.8 ppm) and CH_2 (33.1 ppm) groups (PerkinElmer, 2017). After each adsorption, the ^{13}C MAS NMR spectra of the X-EA-M4 (Fig. 6b-d, up left) showed the same set of signals as the adsorbent, but the signal corresponding to the CH_2 carbon resonated at lower frequencies. The sum of the amount of sodium cations (ICP-MS) and organic cations (TG) desorbed was lower than the amount of heavy metal adsorbed, which could indicate that part of the organic cations was adsorbed as ion pair along with the ions NO_3^- from the solutions of the heavy metals salts. These ions would shield the charge of the methylene group causing the carbon signal to shift.

The ^{13}C MAS NMR spectrum of EA-M2 (Fig. 6a, up right) showed two sets of signals corresponding to the organic cation carbons in parallel bilayer (13.8 ppm and 33.9 ppm) and parallel monolayer arrangement (16.2 ppm and 37.0 ppm) (PerkinElmer, 2017). After the adsorption with Pb^{2+} and Cd^{2+} (Fig. 6b-c, up right), a decrease in the relative intensity of the signals associated with the organic cation arranged in parallel monolayer was observed. This decrease indicated that the adsorption of heavy metals caused the partial removal of the alkyl ammonium chains. In the case of Hg-EA-M2 (Fig. 6d, up right), it was not possible to distinguish carbon signals in the ^{13}C MAS NMR spectrum. The low signal-to-noise ratio of the ^{13}C MAS NMR spectrum indicated that the sample contained a small amount of EA, allowing Hg^{2+} to form internal sphere complexes, as

inferred by TG. Therefore, the two *001* reflections observed by XRD (Fig. 3d, right) corresponded to different hydration states of the heavy metal cation and not to different configurations of the organic cation, as originally postulated.

The functionalization of MEA-M4 was not complete (Osuna et al., 2020) and the presence of sodium in the interlayer produced different environments in the organic cation. The ^{13}C MAS NMR spectra of X-MEA-M4 showed the same set of signals as the initial functionalized mica, but with different relative intensities due to the loss of the organic cation during the adsorption (Fig. 6, down left). The change in intensity was greater in Hg-MEA-M4 since it was the system that desorbed the highest amount of organic cations during the adsorption as previously observed by ICP-MS (Table 4).

The ^{13}C MAS NMR spectrum of MEA-M2 (Fig. 6a, down right) was characterized by four signals that were assigned to two different cations (PerkinElmer, 2017): HS-CH_2-CH_2-NH_3^+ (40 ppm and 23 ppm) and ^+H_2S-CH_2 -CH_2-NH_3^+ (43 ppm and 33 ppm). The ^{13}C MAS NMR spectra after the adsorption of Pb^{2+} and Hg^{2+} in MEA-M2 (Figure 6b and d, right) only showed the carbon signals of the CH_2-NH_3^+ groups. This fact may indicate that the heavy metal adsorption occurred in the thiol groups, causing a widening of the signal and preventing it from being distinguished from noise.

4. Discussion

These as-made micas, Na-M*n*, adsorbed more amount of heavy metals cations than natural clay minerals, Table S2, (Uddin, 2017a). However, Na-M4 adsorbed a lower amount of heavy metal cations than Na-M2 despite its higher CEC, because the electrostatic interaction between the interlayer cations and the surface of the mica increased, hindering their exchange (Pavón et al., 2014, 2013). Thus, the high attraction between the cations and the surface of Na-M4 provoked that the interlayer space did not

421 change regardless the cation charge. However, a new reflection corresponding to a larger
422 basal spacing was observed in the Na-M2 XRD pattern after the adsorption of Cd^{2+} and
423 Hg^{2+}.

424 In general, the order of the adsorbed amounts of each heavy metal was Hg^{2+}>
425 Pb^{2+}> Cd^{2+}, as previously reported by Osuna et al. (Osuna et al., 2019b) for the cation
426 exchange reaction. Hg^{2+} had a greater tendency to form hydroxyl-complexes
427 ($pk_H(Hg^{2+})$=3.4, $pk_H(Pb^{2+})$=7.7 and $pk_H(Cd^{2+})$=10.1) (Hubbard, 2002) which were
428 thermodynamically more stable and were better adsorbed than the hydrated metal cation
429 (James, R O, Healy, 1972).

430 The set of results indicated the presence of precipitates after the adsorption of
431 Pb^{2+}, Cd^{2+} and Hg^{2+} as an additional adsorption mechanism to the cation exchange
432 process.

433 Although the long-range structure of the adsorbents (XRD) remained unchanged,
434 the hydration of the interlayer space depended on the type of the adsorbed metal cation.
435 The adsorption of Cd^{2+} or Hg^{2+} produced an increase in the basal spacing of Na-M*n*. This
436 was due to the fact that both cations had greater hydration enthalpy, in absolute value,
437 than Pb^{2+} ($\Delta H_{hyd}(Pb^{2+})$=-1481 kJ/mol, $\Delta H_{hyd}(Cd^{2+})$=-1807 kJ/mol and $\Delta H_{hyd}(Hg^{2+})$ =-
438 1824 kJ/mol) (Smith, 1977), and, therefore, they had a greater tendency to surround
439 themselves with water molecules (Etci et al., 2010).

440 The XRD patterns of the EA-M*n* after the adsorption of Cd^{2+} and Hg^{2+} showed
441 new reflections attributed to the hydrated heavy metal cations in the interlayer space. As
442 for MEA-M*n*, the adsorption of these two heavy metals did not affect the hydration of
443 MEA-M4 (Fig. 4, left), however, a change in the relative intensities of the *001* reflections
444 in MEA-M2 was observed (Fig. 4, right). The Pb^{2+} adsorption did not produce changes

445 in the basal space of the adsorbents. In general, the amount of adsorbed Pb^{2+}, Cd^{2+} and
446 Hg^{2+} depended on the hydrolysis constants of each metal.

447 The effect of the ammonium group on the adsorption of heavy metals was
448 analyzed thorough the comparison of the adsorption by Na-M*n* and EA-M*n*.
449 Functionalized micas, EA-M*n*, adsorbed a smaller amount of heavy metal than Na-M*n*.
450 Some authors observed that in natural clays, the adsorption capacity of heavy metals
451 decreased after the functionalization with organic cations (Lee et al., 2002; Oyanedel-
452 Craver and Smith, 2006; Uddin, 2017b). In absence of functional groups capable of
453 adsorbing heavy metal cations, such as ammonium, the adsorption occurred by cationic
454 exchange as shown by XRD, TG and MAS NMR. The exchange between heavy metal
455 cations and organic cations was disadvantaged in relation to sodium because organic
456 cations were more strongly adsorbed on mica than Na^{+} (Lee et al., 2002). In addition, the
457 organophilic character of EA-M*n* hindered the adsorption of heavy metal cations.
458 However, the adsorption of Cd^{2+} in both Y-M2 was practically the same and in EA-M4
459 was higher than in Na-M4, probably due to the formation of amorphous precipitates that
460 were not observed by XRD.

461 Finally, the effect of thiol groups on the adsorption was evaluated from the
462 adsorption results obtained by EA-M*n* and MEA-M*n*.

463 ICP-MS data showed that the presence of thiol groups in the organic cation
464 decreased the adsorption of Pb^{2+} and Cd^{2+}, but improved the adsorption of Hg^{2+}. In MEA-
465 M*n,* the adsorption of Pb^{2+} and Cd^{2+} occurred mainly by cation exchange mechanism
466 while the Hg^{2+} adsorption was also at specific sites (thiol groups) (Table 4). The
467 adsorption of mercury cations in the thiol group was favored with respect to the other two
468 heavy metal cations, since Hg^{2+} Gibbs free energy was more negative than that of Pb^{2+}
469 and Cd^{2+} (Brown et al., 1999):

470

$H_2S + M^{2+} \rightarrow MS + 2H^+$

$\Delta G°$ (Hg^{2+}) = -181.6 kJ/mol

$\Delta G°$ (Cd^{2+}) = -45.3 kJ/mol

$\Delta G°$ (Pb^{2+}) = -40.9 kJ/mol

471 Several authors, (do Nascimento et al., 2016; Guerra et al., 2009; Tran et al.,
472 2015a, 2015b) had previously observed that natural clays adsorbed a higher amount of
473 Hg^{2+} after functionalizing them with thiol groups. After the functionalization of
474 motmorillonites and sepiolites with MEA and MPTMS, respectively, their Hg^{2+}
475 adsorption capacity increased and their Pb^{2+} adsorption capacity decreased (Celis et al.,
476 2000).

477 The data obtained from the XRD, ICP-MS and ^{13}C MAS NMR spectroscopy
478 indicated that the loss of organic cations during the adsorption was lower in MEA-M*n*
479 than in EA-M*n*, so thiol groups increased the adsorption strength of the organic cation
480 and hindered cation exchange reaction. Thus, the presence of thiol groups in the organic
481 chain provided specific sites for the Hg^{2+} adsorption, but hindered the adsorption of Pb^{2+}
482 and Cd^{2+}.

483

484 **5. Conclusions**

485 The efficient adsorption of heavy metal cations in water from both as-made and
486 functionalized micas has been demonstrated, being the efficiency higher in Y-M2 than in
487 Y-M4. In all the adsorbents, a higher amount of Hg^{2+} is adsorbed, followed by Pb^{2+}, and,
488 finally Cd^{2+}.

489 In general, the functionalization of micas decreases the amount of adsorbed heavy
490 metal, except for Hg-MEA-M*n*, since the presence of thiol groups generates specific
491 adsorption sites that improves their adsorption capacity.

In summary, the best adsorbent for Pb^{2+} and Cd^{2+} is Na-M2, and, in the case of Hg^{2+}, the best adsorbent is the MEA-M2. The adsorption amount of Pb^{2+} and Cd^{2+} by Na-M2 is 3373.3 meq/kg and 2263.0 meq/kg, respectively, and, 4918.6 meq Hg^{2+} are adsorbed per 1 kg of MEA-M2, being the adsoption capacity of these micas ten time higher than the capacity of the reported natural clay minerals.

Acknowledgements

The authors would like to thank the Junta de Andalucía (Spain) and FEDER (Proyecto de Excelencia de la Junta de Andalucía, project P12-FQM-567), to the Spanish State Program R+D+I oriented societal challenges and FEDER (Project MAT2015-63929-R) for financial support. F.J. Osuna thanks his grant to the training researcher program associated to the excellence project of the Junta de Andalucía (P12-FQM-567). Dr. Pavón thanks the University of Seville for the financial support of her current contract from VI PPIT-US program.

References

Alba, M.D., Castro, M.A., Naranjo, M., Pavón, E., 2006. Hydrothermal reactivity of Na-n-micas (n = 2, 3, 4). Chem. Mater. 18, 2867–2872.

Bailey, S.E., Olin, T.J., Bricka, R.M., Adrian, D.D., 1999. A review of potentially low-cost sorbents for heavy metals. Water Res. 33, 2469–2479.

Balasubramanian, N., Ahamed, A.J., 2000. Adsorption dynamics - temperature effect on adsorption of lead(II) species onto lignite surface. J. Indian Chem. Soc. 77, 11–13.

Bhattacharyya, K.G., Sen Gupta, S., 2008. Adsorption of a few heavy metals on natural and modified kaolinite and montmorillonite: A review. Adv. Colloid Interface Sci. 140, 114–131.

517 Brown, J., Mercier, L., Pinnavaia, T.J., 1999. Selective adsorption of Hg2+ by thiol-
518 functionalized nanoporous silica. Chem. Commun. 69–70.
519 Celis, R., Hermosin, M.C., Cornejo, J., 2000. Heavy metal adsorption by functionalized
520 clays. Environ. Sci. Technol. 34, 4593–4599.
521 Cruz-Guzman, M., Celis, R., Hermosin, M.C., Koskinen, W.C., Nater, E.A., Cornejo, J.,
522 2006. Heavy metal adsorption by montmorillonites modified with natural organic
523 cations. Soil Sci. Soc. Am. J. 70, 215–221.
524 do Nascimento, F.H., de Souza Costa, D.M., Masini, J.C., 2016. Evaluation of thiol-
525 modified vermiculite for removal of Hg(II) from aqueous solutions. Appl. Clay Sci.
526 124, 227–235.
527 Etci, O., Bektas, N., Oncel, M.S., 2010. Single and binary adsorption of lead and cadmium
528 ions from aqueous solution using the clay mineral beidellite. Environ. Earth Sci. 61,
529 231–240.
530 Ezzat, H., Menazea, A.A., Omara, W., Basyouni, O.H., Helmy, S.A., Mohamed, A.A.,
531 Tawfik, W., Ibrahim, M., 2020. DFT: B3LYP/LANL2DZ Study for the Removal of
532 Fe, Ni, Cu, As, Cd and Pb with Chitosan. Biointerface Res. Appl. Chem. 10, 7002–
533 7010.
534 Fahim, R.B., Kolta, G.A., 1970. Thermal decomposition of hydrated Cadmium oxide. J.
535 Phys. Chem. 74, 2501–2507.
536 Farid, I.M., Abbas, M.H.H., Bassouny, M.A., Gameel, A., Abbas, H.H., 2020. Indirect
537 Impacts of Irrigation with Low Quality Water on The Environmental Safety.
538 Egyotian J. Soil Sci. 60, 1–15.
539 Figueroa, A., Cameselle, C., Gouveia, S., Hansen, H.K., 2016. Electrokinetic treatment
540 of an agricultural soil contaminated with heavy metals. J. Environ. Sci. Heal. Part
541 A-Toxic/Hazardous Subst. Environ. Eng. 51, 691–700.

García-Jiménez, M.J., Cota, A., Osuna, F.J., Pavón, E., Alba, M.D., 2016. Influence of temperature and time on the Eu3+ reaction with synthetic Na-Mica-n (n=2 and 4). Chem. Eng. J. 284, 1174–1183.

Grim, R.E., 1968. Clay Mineralogy. New York.

Guerra, D.L., Santos, M.R.M.C., Airoldi, C., 2009. Mercury Adsorption on Natural and Organofunctionalized Smectites - Thermodynamics of Cation Removal. J. Braz. Chem. Soc. 20, 594–603.

Ho, Y S, Ng, J C Y, McKay, G., 2001. Removal of lead(II) from effluents by sorption on peat using second-order kinetics. Sep. Sci. Technol. 36, 241–261.

Ho, Y.S., 2003. Removal of copper ions from aqueous solution by tree fern. Water Res. 37, 2323–2330.

Hu, G, Liu, G, Wu, D , Fu, B., 2018. Geochemical behavior of hazardous volatile elements in coals with different geological origin during combustion. Fuel 233, 361–376.

Hubbard, A.T., 2002. Encyclopedia of surface and colloid science. Vol. 1. CRC Press.

Inglezakis, V.J., Stylianou, M.A., Gkantzou, D., Loizidou, M.D., 2007. Removal of Pb(II) from aqueous solutions by using clinoptilolite and bentonite as adsorbents. Desalination 210, 248–256.

James, R O, Healy, T.W., 1972. Adsorption of hydrolyzable metal-ions at oxide-water interface .3. Thermodynamic model of adsorption. J. Colloid Interface Sci. 40, 65-.

Kodama, T., Komarneni, S., 1999. Na-4-mica: Cd2+, Ni2+, Co2+, Mn2+ and Zn2+ ion exchange. J. Mater. Chem. 9, 533–539.

Lee, J.J., Choi, J., Park, J.W., 2002. Simultaneous sorption of lead and chlorobenzene by organobentonite. Chemosphere 49, 1309–1315.

Lin, S.H., Juang, R.S., 2002. Heavy metal removal from water by sorption using

surfactant-modified montmorillonite. J. Hazard. Mater. 92, 315–326.

Malferrari, D., Brigatti, M.F., Laurora, A., Medici, L., Pini, S., 2006. Thermal behavior of Cu(II)-, Cd(II)-, and Hg(II)-exchanged montmorillonite complexedwith cysteine. J. Therm. Anal. Calorim. 86, 365–370.

Malferrari, D., Brigatti, M.F., Laurora, A., Pini, S., Medici, L., 2007. Sorption kinetics and chemical forms of Cd(II) sorbed by thiol-functionalized 2 : 1 clay minerals. J. Hazard. Mater. 143, 73–81.

Mathur, A., Rupainwar, D.C., 1988. Removal of lead from polluted waters by adsorption on fly ash. Asian Environ. 10, 19–25.

Mercier, L, Detellier, C., 1995. Preparation, characterization and applications as heavy-metals sorbent of covalently grafted thiol functionalities on the interlamellar surface of montmorillonite. Environ. Sci. Technol. 29, 1318–1323.

Mittal, A., Ahmad, R., Hasan, I., 2016. Biosorption of Pb2+, Ni2+ and Cu2+ ions from aqueous solutions by L-cystein-modified montmorillonite-immobilized alginate nanocomposite. Desalin. Water Treat. 57, 17790–17807.

Naranjo, M., Castro, M.A., Cota, A., Osuna, F.J., Pavón, E., Alba, M.D., 2015. Synthesis temperature effect on Na-Mica-4 crystallinity and heteroatom distribution. Microporous Mesoporous Mater. 204, 282–288.

Naranjo, M., Castro, M.A., Cota, A., Pavón, E., Pazos, M.C., Alba, M.D., 2014. A new route of synthesis of Na-Mica-4 from sodalite. Microporous Mesoporous Mater. 186, 176–180.

NJDEP, 2014. Technical Guidance on the Capping of Sites Undergoing Remediation.

Osuna, F.J., Cota, A., Fernandez, M.A., Pavon, E., Torres Sanchez, R.M., Alba, M.D., 2019a. Influence of framework and interlayer on the colloidal stability of design swelling high-charged micas. Colloids Surfaces A-Physicochemical Eng. Asp. 561,

592 32–38.
593 Osuna, F.J., Cota, A., Pavón, E., Carolina Pazos, M., Alba, M.D., 2018. Cesium
594 adsorption isotherm on swelling high-charged micas from aqueous solutions: Effect
595 of temperature. Am. Mineral. 103.
596 Osuna, F.J., Pavon, E., Alba, M.D., 2020. An insight on the design of mercapto
597 functionalized swelling brittle micas. J. Colloid Interface Sci. 561, 533–541.
598 Osuna, F.J., Pavon, E., Alba, M.D., 2019b. Design swelling micas: Insights on heavy
599 metals cation exchange reaction. Appl. Clay Sci. 182, 105298.
600 Oyanedel-Craver, V.A., Smith, J.A., 2006. Effect of quaternary ammonium cation
601 loading and pH on heavy metal sorption to Ca bentonite and two organobentonites.
602 J. Hazard. Mater. 137, 1102–1114.
603 Pavón, E., Castro, M.A., Cota, A., Osuna, F.J., Pazos, M.C., Alba, M.D., 2014. Interaction
604 of hydrated cations with mica-n (n = 2, 3 and 4) surface. J. Phys. Chem. C 118,
605 2115–2123.
606 Pavón, E., Castro, M.A., Naranjo, M., Orta, M.M., Pazos, M.C., Alba, M.D., 2013.
607 Hydration properties of synthetic high-charge micas saturated with different cations:
608 An experimental approach. Am. Mineral. 98, 394–400.
609 Pazos, M.C., Castro, M.A., Cota, A., Osuna, F.J., Pavón, E., Alba, M.D., 2017. New
610 insights into surface-functionalized swelling high charged micas: Their adsorption
611 performance for non-ionic organic pollutants. J. Ind. Eng. Chem. 52, 179–186.
612 Periasamy, K, Namasivayam, C., 1994. Process-development for removal and recovery
613 of cadmium from waste-water by a low-cost adsorbent - Adsorption rates and
614 equilibrium studies. Ind. Eng. Chem. Res. 33, 317–320.
615 PerkinElmer, 2017. ChemDraw Proffesional 16.0.1.4/77.
616 Praus, P., Motakova, M., Ritz, M., 2012. Montmorillonite ion exchanged by mercury (II).

617 Acta Geodyn. Geomater. 9, 63–70.
618 Shah, D., Fytas, G., Vlassopoulos, D., Di, J., Sogah, D., Giannelis, E.P., 2005. Structure
619 and dynamics of polymer-grafted clay suspensions. Langmuir 21, 19–25.
620 Shaikh, T.M.A., 2020. Adsorption of Pb(II) from wastewater by natural and synthetic
621 adsorbents. Biointerface Res. Appl. Chem. 10, 6522–6539.
622 Shaikhiev, I.G., Kraysman, N. V, Sverguzova, S. V, Spesivtseva, S.E., Yarothckina,
623 A.N., 2020. Fish Scales as a Biosorbent of Pollutants from Wastewaters and Natural
624 Waters (a Literature Review). Biointerface Res. Appl. Chem. 10, 6893–6905.
625 Shen, Z., Jin, F., O'Connor, D., Hou, D., 2019. Solidification/Stabilization for Soil
626 Remediation: An Old Technology with New Vitality. Environ. Sci. Technol. 53,
627 11615–11617.
628 Sierra, C., Gallego, J.R., Afif, E., Menendez-Aguado, J.M., Gonzalez-Coto, F., 2010.
629 Analysis of soil washing effectiveness to remediate a brownfield polluted with pyrite
630 ashes. J. Hazard. Mater. 180, 602–608.
631 Smith, D.W., 1977. Ionic hydration enthalpies. J. Chem. Educ. 54, 540–542.
632 Sun, M., Wang, T., Xu, X., Zhang, L., Li, J., Shi, Y., 2020. Ecological risk assessment of
633 soil cadmium in China's coastal economic development zone: a meta-analysis.
634 Ecosyst. Heal. Sustain. 6, Article: 1733921.
635 Tran, H.H., Roddick, F.A., O'Donnell, J.A., 1999. Comparison of chromatography and
636 desiccant silica gels for the adsorption of metal ions - I. adsorption and kinetics.
637 Water Res. 33, 2992–3000.
638 Tran, L., Wu, P., Zhu, Y., Liu, S., Zhu, N., 2015a. Comparative study of Hg(II) adsorption
639 by thiol- and hydroxyl-containing bifunctional montmorillonite and vermiculite.
640 Appl. Surf. Sci. 356, 91–101.
641 Tran, L., Wu, P., Zhu, Y., Yang, L., Zhu, N., 2015b. Highly enhanced adsorption for the

642 removal of Hg(II) from aqueous solution by
643 Mercaptoethylamine/Mercaptopropyltrimethoxysilane functionalized vermiculites.
644 J. Colloid Interface Sci. 445, 348–356.
645 Uddin, M.K., 2017a. A review on the adsorption of heavy metals by clay minerals, with
646 special focus on the past decade. Chem. Eng. J. 308, 438–462.
647 Uddin, M.K., 2017b. A review on the adsorption of heavy metals by clay minerals, with
648 special focus on the past decade. Chem. Eng. J. 308, 438–462.
649 Ugochukwu, N., Mohamed, I., Ali, M., Iqbal, J., Fu, Q., Zhu, J., Jiang, G., Hu, H., 2013.
650 Impacts of inorganic ions and temperature on lead adsorption onto variable charge
651 soils. Catena 109, 103–109.
652 Volesky, B., 1990. Biosorption of Heavy Metals, 4th ed. CRC Press.
653 Wu, P., Zhang, Q., Dai, Y., Zhu, N., Dang, Z., Li, P., Wu, J., Wang, X., 2011. Adsorption
654 of Cu(II), Cd(II) and Cr(III) ions from aqueous solutions on humic acid modified
655 Ca-montmorillonite. Geoderma 164, 215–219.
656 Yang, Z., Dong, Y., Li, Z., 2020. Acid mine drainage remediation with simulated
657 permeable reactive barrier filled with fly ash and its composite materials as reactive
658 media. Energy Sources Part A-Recovery Util. Environ. Eff. 42, 1–14.
659 Yuan, J., Lu, Y., Wang, Chenchen, Cao, X., Chen, C., Cui, H., Zhang, M., Wang, Cong,
660 Li, X., Johnson, A.C., Sweetnnan, A.J., Du, D., 2020. Ecology of industrial pollution
661 in China. Ecosyst. Heal. Sustain. 6, Article: 1779010.
662 Zhang, Y., Wu, D., Wang, C., Fu, X., Wu, G., 2020. Impact of coal power generation on
663 the characteristics and risk of heavy metal pollution in nearby soil. Ecosyst. Heal.
664 Sustain. 6, Article: 1787092.
665
666

667

Table 1.
Water content of samples before and after adsorption.

Adsorbent	mol water/kg clay				
	25 °C -230 °C			25 °C -150 °C	
	raw	Pb^{2+}	Cd^{2+}	raw	Hg^{2+}
Na-M2	3.9	3.5	5.9	3.8	2.4
EA-M2	2.2	3.8	6.2	1.8	2.4
MEA-M2	3.4	3.7	4.0	3.1	2.9
Na-M4	3.6	3.3	3.9	3.5	2.8
EA-M4	3.1	1.6	2.9	2.5	2.5
MEA-M4	2.3	2.4	2.4	1.8	1.8

668

669

670

Table 2.
Temperatures of vaporization of Hg^{2+} adsorbed in organic chain (T_1), Hg^{2+} on external sphere complex (T_3) and Hg^{2+} on internal sphere complex (T_4), and, organic decomposition (T_2).

	T (ºC)			
	T_1	T_2	T_3	T_4
Hg-EA-M2	235	430	350	570
Hg-EA-M4	220	290 445	350	620
Hg-MEA-M2	200	270	340	600
Hg-MEA-M4	200	270	340	-

671

672

673

674

675

676

677

678

679

680

Table 3.
Organic matter content of mica from TG and ICP-MS analysis.

	X-EA-M2	X-EA-M4	X-MEA-M2		X-MEA-M4	
	TG (meq/kg)	TG (meq/kg)	TG (meq/kg)	ICP-MS (meq/kg)	TG (meq/kg)	ICP-MS (meq/kg)
raw	2419.7	3374.1	2432.8	3010 ±9	2818.1	3410 ±22
Pb^{2+}	852.6	3141.7	1636.5	1503 ±3	2646.8	2627 ±3
Cd^{2+}	758.2	1793.1	2402.9	2180 ±19	2820.7	2756 ±18
Hg^{2+}	6817.9	7072.3	7156.9	1606 ±5	6961.2	2072 ±9

681

682

Table 4.
Amount of adsorbed heavy metal cations (C_s (X^{2+})) and desorbed interlayer cation (C_{des} (EA/MEA+Na^+)).

	X	C_s (X^{2+}) (meq/kg)	C_{des} (EA/MEA+Na^+) (meq/kg)
X-EA-M2	Pb^{2+}	2356.2	1823.9
	Cd^{2+}	2167.3	1984.4
	Hg^{2+}	3448.8	--
X-MEA-M2	Pb^{2+}	1249.9	1631
	Cd^{2+}	315.9	968.1
	Hg^{2+}	4918.6	1786.9
X-EA-M4	Pb^{2+}	1094.8	574.61
	Cd^{2+}	1952.3	1819.7
	Hg^{2+}	2338.5	--
X-MEA-M4	Pb^{2+}	780.9	1019.8
	Cd^{2+}	725.3	821.0
	Hg^{2+}	4105.7	1677.5

683

684 **FIGURE CAPTION**

685 **Fig. 1.** Amount of desorbed Na^{+} (grey) and adsorbed Pb^{2+} (orange), Cd^{2+} (blue), and, Hg^{2+}

686 (green). Red dash line indicates the CEC of the adsorbent.

687 **Fig. 2.** XRD of Na-M*n* (*n*=4, left, and *n*=2, right) before (a) and after adsorption of: b)

688 Pb^{2+}, c) Cd^{2+}, and, d) Hg^{2+}. h= $Hg(NO_3)_2 \cdot 3H_2O$ (PDF 00-031-0855).

689 **Fig. 3.** XRD of EA-M*n* (*n*=4, left, and *n*=2, right) before (a) and after adsorption of: b)

690 Pb^{2+}, c) Cd^{2+}, and, d) Hg^{2+}.

691 **Fig. 4.** XRD of MEA-M*n* (*n*=4, left, and *n*=2, right) before (a) and after adsorption of: b)

692 Pb^{2+}, c) Cd^{2+}, and, d) Hg^{2+}.

693 **Fig. 5.** ^{23}Na MAS NMR spectra of adsorbents X-M*n* (*n*=4, upper, and *n*=2, bottom; X=Na,

694 left, X=EA, middle, and, X=MEA, right) before (a) and after adsorption of: b) Pb^{2+}, c)

695 Cd^{2+}, and, d) Hg^{2+}.

696 **Fig. 6.** ^{13}C MAS NMR spectra of adsorbents X-M*n* (*n*=4, upper, and *n*=2, bottom; X=EA,

697 left, and, X=MEA, right) before (a) and after adsorption of: b) Pb^{2+}, c) Cd^{2+}, and, d) Hg^{2+}.

698

699 **Fig. 1**

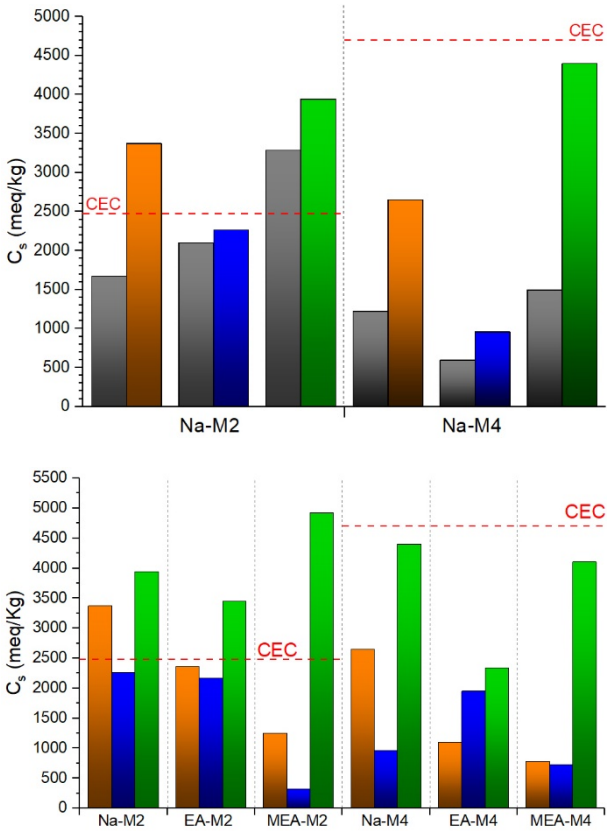

700

701

702

703 **Fig. 2**

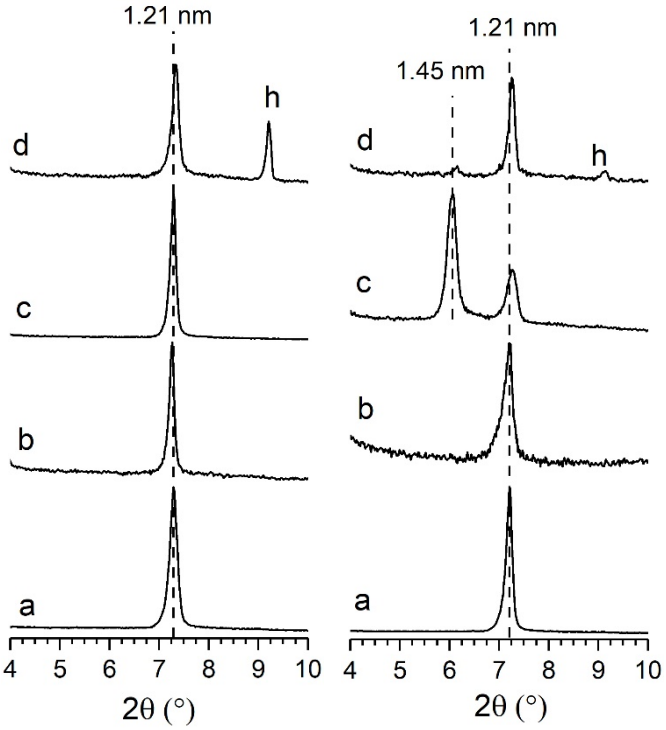

704

705 **Fig. 3**

706

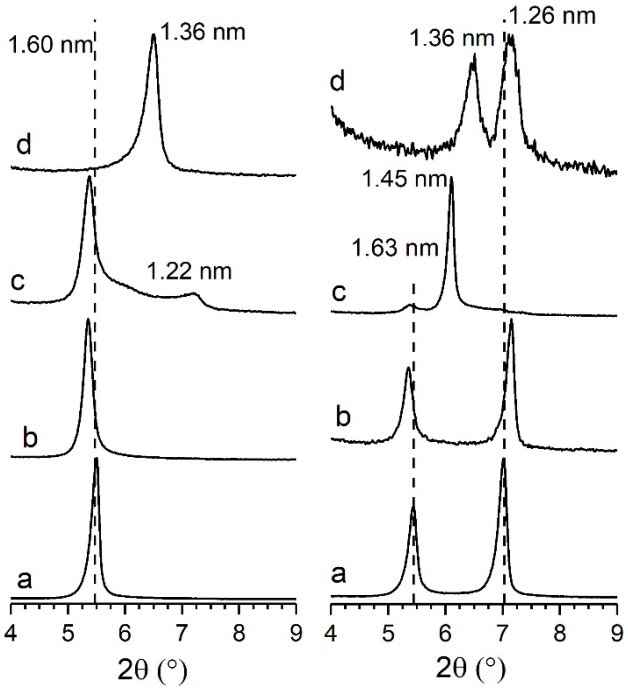

707

708 **Fig. 4**

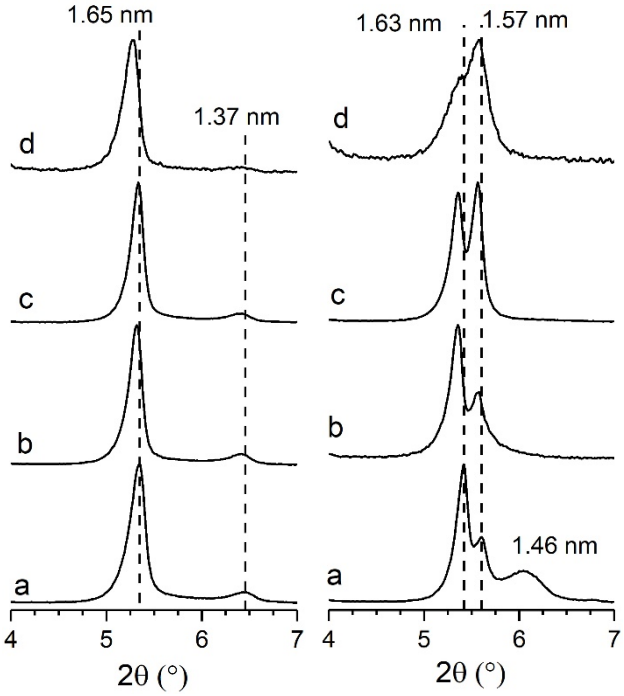

709

710 **Fig. 5**

711

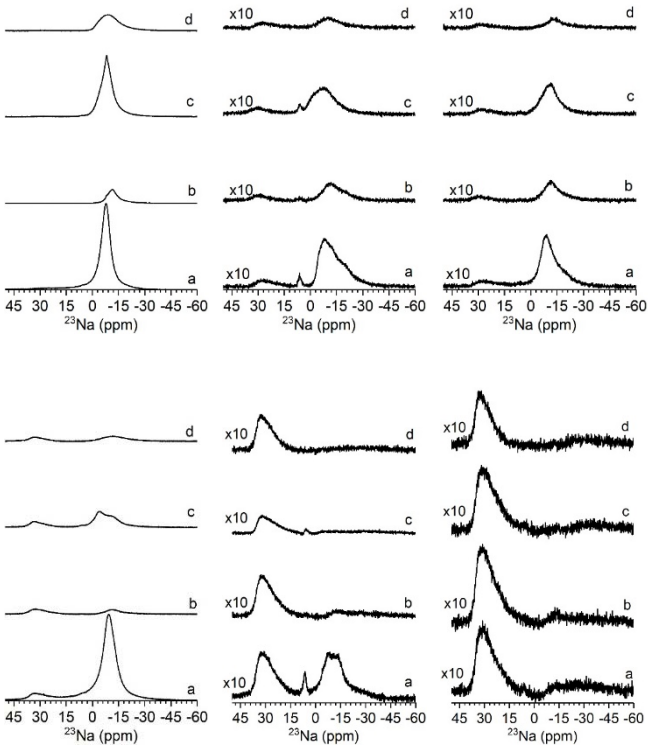

712

713 **Fig. 6**

714

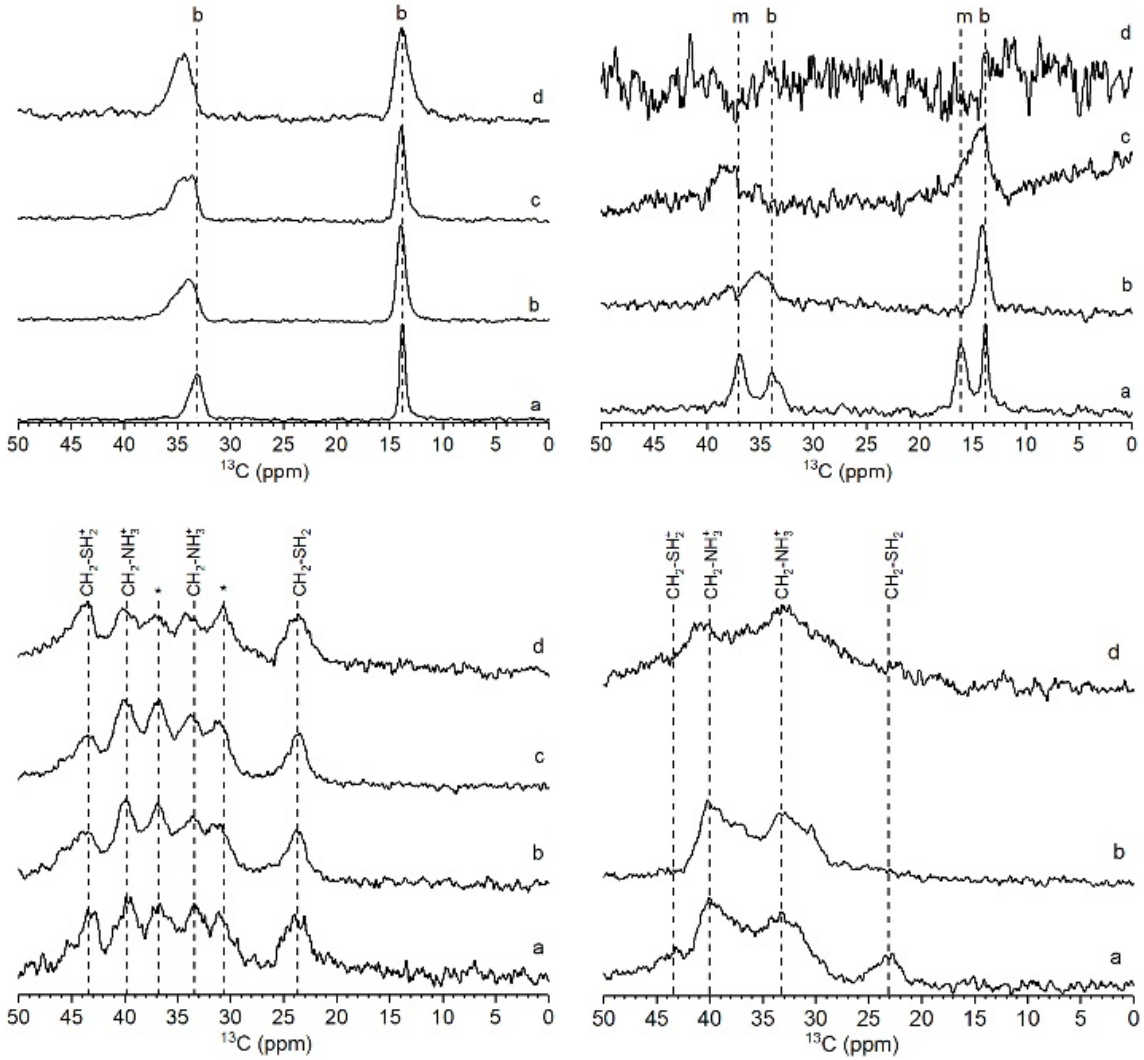

715

716